Available online at www.sciencedirect.com
ScienceDirect
Comput. Methods Appl. Mech. Engrg. 340 (2018) 798–823
Computer methods in applied mechanics and engineering
www.elsevier.com/locate/cma

Multi-material continuum topology optimization with arbitrary volume and mass constraints

Emily D. Sanders[a], Miguel A. Aguiló[b], Glaucio H. Paulino[a,*]

[a] *School of Civil and Environmental Engineering, Georgia Institute of Technology, 790 Atlantic Drive, Atlanta, GA, 30332, United States*
[b] *Simulation and Modeling Sciences, Sandia National Laboratories, P.O. Box 5800, Albuquerque, NM 87185, United States*

Received 29 April 2017; received in revised form 13 January 2018; accepted 17 January 2018
Available online 7 February 2018

Abstract

A framework is presented for multi-material compliance minimization in the context of continuum based topology optimization. We adopt the common approach of finding an optimal shape by solving a series of explicit convex (linear) approximations to the volume constrained compliance minimization problem. The dual objective associated with the linearized subproblems is a separable function of the Lagrange multipliers and thus, the update of each design variable is dependent only on the Lagrange multiplier of its associated volume constraint. By tailoring the ZPR design variable update scheme to the continuum setting, each volume constraint is updated independently. This formulation leads to a setting in which sufficiently general volume/mass constraints can be specified, i.e., each volume/mass constraint can control either all or a subset of the candidate materials and can control either the entire domain (global constraints) or a sub-region of the domain (local constraints). Material interpolation schemes are investigated and coupled with the presented approach. The key ideas presented herein are demonstrated through representative examples in 2D and 3D.

Keywords: Topology optimization; Multi-material; Volume constraints; Mass constraints; ZPR update; Additive manufacturing

1. Introduction

The multi-material, volume-constrained, compliance minimization problem considered here is stated (in discretized form) as:

$$\begin{aligned} \min_{\mathbf{z}_1,\ldots,\mathbf{z}_m} \quad & J = \mathbf{f}^T \mathbf{u}\left(\mathbf{z}_1,\ldots,\mathbf{z}_m\right) \\ \text{s.t.} \quad & g_j = \sum_{i\in\mathcal{G}_j}\sum_{e\in\mathcal{E}_j} \hat{z}_i^e V^e \le V_j^{max}, \qquad j = 1,\ldots,N_c \\ & 0 \le z_i^e \le 1, \qquad i = 1,\ldots,m; \quad e = 1,\ldots,N \\ \text{with} \quad & \mathbf{K}\left(\mathbf{z}_1,\ldots,\mathbf{z}_m\right)\mathbf{u}\left(\mathbf{z}_1,\ldots,\mathbf{z}_m\right) = \mathbf{f} \end{aligned} \tag{1}$$

* Corresponding author.
E-mail address: paulino@gatech.edu (G.H. Paulino).

https://doi.org/10.1016/j.cma.2018.01.032
0045-7825/

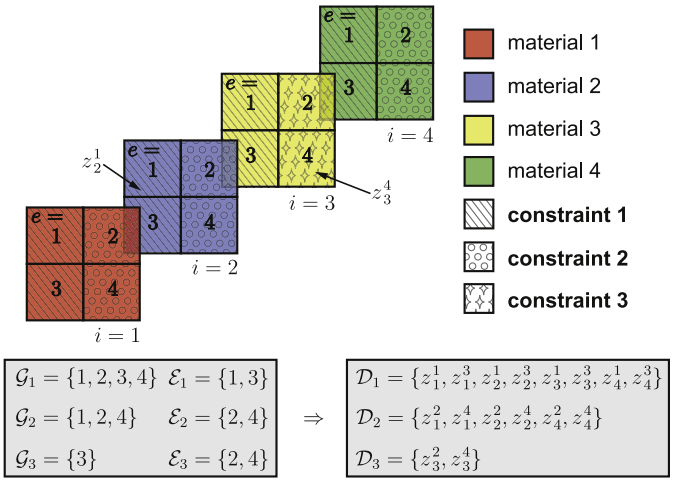

Fig. 1. Illustration of the material and constraint specification for a 2×2 mesh with four candidate materials and three constraints, each controlling a subset of the candidate materials in a sub-region of the domain. The set of material indices, $\mathcal{G}_j$, the set of element indices, $\mathcal{E}_j$, and the set of design variables, $\mathcal{D}_j$, associated with each constraint are indicated for constraints $j = 1, \ldots, 3$ (color online).

where $\mathbf{z}_1, \ldots, \mathbf{z}_m$ represent m density fields defined at N points in the problem domain for each of the m candidate materials, J is the structural compliance, g_j are the volume constraints, $\mathcal{G}_j$ is the set of material indices associated with constraint j, $\mathcal{E}_j$ is the set of element indices associated with constraint j, $\hat{z}_i^e$ is the filtered density of material i in element e, V^e is the volume of element e, V_j^{max} is the material volume limit corresponding to constraint j, N_c is the total number of volume constraints, and $\mathbf{K}$, $\mathbf{u}$, and $\mathbf{f}$ are the stiffness matrix, displacement vector, and force vector, respectively, of the associated elastostatics problem that has been discretized into finite elements.

For illustration purposes, key characteristics of the problem definition and formulation in (1) are highlighted in Fig. 1, which shows a 2×2 mesh with four candidate materials and three constraints. Note that there are four sets of design variables, one for each of the four candidate materials. Additionally, the volume constraints are specified in a very general way. In accordance with (1), each constraint may control the selection of all or a subset of the candidate materials and may be specified for the entire domain or for a sub-region of the domain, with the requirement that each design variable is associated with only a single constraint. For the illustrative example in Fig. 1, the set of material indices, $\mathcal{G}_j$, the set of element indices, $\mathcal{E}_j$, and the resulting set of design variables, $\mathcal{D}_j = \{z_i^e : i \in \mathcal{G}_j, e \in \mathcal{E}_j\}$, associated with each constraint ($j = 1, \ldots, 3$) are indicated in the gray boxes at the bottom of the figure. Further, Fig. 2 illustrates three general ways in which materials may be distributed using this framework. For example, all candidate materials may be available to the entire domain (Fig. 2(a)), each candidate material may be available to a different sub-region of the domain (Fig. 2(b)), or multiple candidate materials may be available to the same sub-region of the domain (Fig. 2(c)).

Volume constraints were specified in this general way by Zhang et al. [1] in the context of ground structures and handled using the ZPR design variable update scheme (named after the authors Zhang–Paulino–Ramos Jr. and pronounced "zipper"). The ZPR design variable update scheme takes advantage of the separable nature of the Lagrangian associated with the linearized subproblems of (1), allowing the design variables to be updated for each constraint in series or in parallel (i.e., the constraints are independent of one another). This tailored design variable update scheme is robust and, thus, enables the formulation to efficiently accommodate an arbitrary number of candidate materials and many volume/mass constraints (possibly hundreds).

This work focuses on linear elastic materials in a continuum setting. If these materials are also isotropic the optimizer will, in general, select the stiffest of the candidate materials associated with each volume constraint. By including additional information about each material (e.g., mass density or cost), multiple materials may appear in the design [2–6]. For example, a scale factor, γ_i, for each material can be added to the constraint in (1) such that it becomes:

$$g_j = \sum_{i \in \mathcal{G}_j} \sum_{e \in \mathcal{E}_j} \hat{z}_i^e \gamma_i V^e \leq M_j^{max} \qquad j = 1, \ldots, N_c. \tag{2}$$

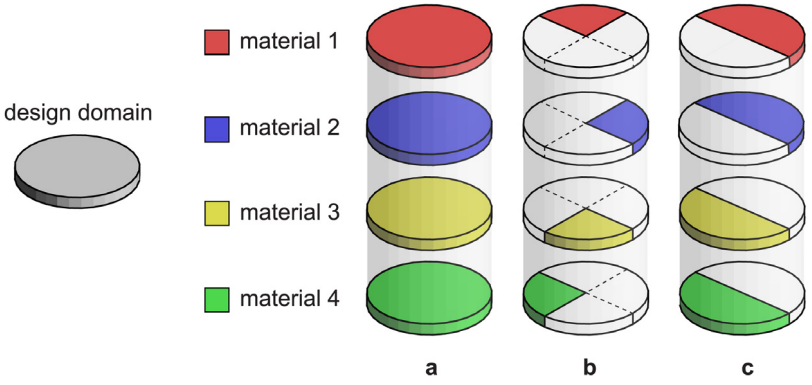

Fig. 2. Illustration of three general ways that multiple materials may be arranged in a design domain when using the framework in (1) for specifying volume constraints: (a) all candidate materials are available to the entire domain; (b) each candidate material is available to a separate sub-region of the domain; (c) multiple candidate materials are available to the same sub-region of the domain (color online).

The scale factor, γ_i, can be thought of as a mass density or cost of material i and M_j^{max} as the mass or monetary limit associated with constraint j. For brevity, the constraint in (2) is interpreted here as a mass constraint rather than a cost constraint. It is noted that when $\gamma_i = 1 \ \ \forall i$, the standard volume constraints of (1) are recovered. In all cases, the optimizer will tend to use all available material such that the volume and/or mass constraints are satisfied in equality.

The remainder of this manuscript is organized as follows: In Section 2, multi-material topology optimization is motivated and related work in the field is reviewed. In Section 3, the problem setting and formulation are provided, the material interpolation scheme is discussed, and the sensitivities are derived. The ZPR update scheme is tailored to the continuum in Section 4. Section 5 includes some details related to implementation of the multi-material framework. Four numerical examples are provided in Section 6 to demonstrate the capabilities and potential shortcomings of the proposed approach. Finally, in Section 7, conclusions are provided.

2. Motivation and related work

With the rapid advancement of additive manufacturing technologies in recent years, it has become increasingly feasible to fabricate arbitrary geometries such as designs derived from topology optimization (see e.g., [7,8]). Until recently, most additive manufacturing technologies have been limited to fabricating designs from a single material, leading to parts with little functional capability. Multi-material 3D printing is only a budding technology, but will certainly lead to increasingly functional designs. For instance, Gaynor et al. [9] manufactured compliant mechanism designs based on three-phase (2 solid phases plus void) topology optimization using the PolyJet additive manufacturing technology, which can print bulk materials covering a wide range of elastic moduli [10]. Even using single material printers, functional designs have been fabricated by varying the microstructure throughout the print to achieve varying elastic properties [11].

Perhaps due to the excitement surrounding additive manufacturing, the number of publications related to multi-material topology optimization in the continuum setting is growing. The great majority of work in density-based topology optimization considering multiple material phases is based on some extension of the Solid Isotropic Material with Penalization (SIMP) interpolation scheme, which uses a power law to penalize intermediate densities and achieve designs with distinct solid and void regions [12,13]. For two-material (no void) topology optimization of materials with extreme thermal expansion, Sigmund and Torquato [14] use a single design variable to interpolate between two material phases. The approach has also been used to design, for example, multi-physics actuators [15], piezocomposites [16–18], and functionally graded structures with optimal eigenfrequencies [19]. Sigmund and Torquato [14] also proposed a three-phase extension of SIMP characterized by a topology design variable that controls the material/void distribution and a second design variable that interpolates between two solid material phases. Although this "three-phase mixing scheme" has been extended further to incorporate up to m candidate materials [20], some authors claim that designs tend to get stuck in local minima when the number of materials exceeds three solid phases [5,20]. Actually, most results in the literature for multi-material topology optimization using this "m-phase mixing scheme" have been limited to two [2,9,21] or three [5] solid phases plus void.

Other material interpolation schemes that are better equipped to handle greater than three solid phases have also been proposed. For example, in the context of composite design via fiber orientation optimization, the Discrete Material Optimization (DMO) technique was proposed to consider an arbitrary number of materials, each characterized by a discrete fiber orientation [20,22]. The DMO interpolation schemes are typically also an extension of SIMP, but differ from the "m-phase mixing scheme" discussed above in that each design variable represents the density of a single material. Gao and Zhang [2] compared the DMO interpolation schemes to the "m-phase mixing scheme" and found that DMO is able to reach superior designs, even in cases considering only two solid phases plus void and a single mass constraint. However, the DMO interpolation methods do not inherently prevent the sum of material densities at a point from exceeding one as the "m-phase mixing scheme" does. To enforce this property when using DMO, Hvejsel and Lund [23] and Hvejsel et al. [24] impose a large system of sparse linear constraints and Hvejsel et al. [24] further enforces a quadratic constraint to penalize material mixing.

Tavakoli and Mohseni [25] use a DMO interpolation scheme coupled with an alternating active-phase (AAP) algorithm in which designs containing up to m material phases are achieved by performing m binary material phase updates in an inner loop of each outer optimization iteration. Implementing this approach essentially amounts to adding a loop over an existing two-phase topology optimization code. Although this approach is seemingly flexible enough to accommodate an arbitrary number of candidate materials, it may be difficult to obtain converged solutions for more than five materials using the code from reference [25]. Additionally, resulting designs depend on the order of materials being updated, which may prevent the method from being applicable to problems considering materials with more general constitutive behavior (e.g., nonlinear or anisotropic materials). Furthermore, the AAP algorithm leads to an increase in the number of finite element solves by a factor of the number of candidate materials times the number of specified inner iterations, and thus, may not scale to large problems. Despite these drawbacks, a number of authors have adopted the AAP algorithm: Park and Sutradhar [26] couple it with multiresolution topology optimization [27–29] to solve multi-material problems in three dimensions, Lieu and Lee [30] couple it with multiresolution topology optimization and isogeometric analysis [31] to improve computational efficiency; Doan and Lee [32] use it for problems with additional buckling load factor constraints; and Chau et al. [33] use it with polygonal finite elements and adaptive mesh refinement.

A pitfall of the DMO approaches is that the number of design variables scales linearly with the number of candidate materials. Yin and Ananthasuresh [34] propose a peak function material interpolation method in which the number of design variables remains constant as the number of candidate materials increases. In their approach, each material has a mean and a standard deviation and, by using a normal distribution function, a distinct material is selected when the density design variable is equal to the mean of that material. A color level-set approach was also proposed by Wang and Wang [35] in which only m level-set functions are needed to obtain designs with 2^m materials. The method has been applied for compliant mechanism design [36] and in problems considering stress constraints [37]. Multi-material designs have also been achieved using phase-field methods by e.g., Wang and Zhou [38], Zhou and Wang [39], Tavakoli [40], and Wallin et al. [41]; and using evolutionary methods by e.g., Huang and Xie [42].

Although the number of design variables scales linearly with the number of candidate materials and pointwise densities may exceed one, the DMO interpolations lead to linear and variable separable volume/mass constraints. Thus, the following observation by Zhang et al. [1] can be exploited: multiple linear volume constraints lead to a separable Lagrangian function, allowing the design to be updated for each volume/mass constraint independently (i.e., order-independent updates) using the ZPR update scheme [1]. The observation facilitates sufficient flexibility in the problem statement in that volume/mass constraints can be specified to control either all or a subset of the candidate materials in either all or a subset of the design domain (see (1)). The update of each design variable is dependent only on the Lagrange multiplier of its associated volume constraint (no cross-term dependency). As such, the approach is straightforward to implement and the number of finite element solves remains constant as the number of constraints increases. Zhang et al. [1] applied the idea to the design of truss structures with possibly nonlinear materials and here the ZPR scheme is tailored to the continuum setting.

3. Formulation

Multi-material topology optimization for problems in linear elastostatics aims to find the set of material points, $\omega = \{\mathbf{X} \in \mathbb{R}^{n_d}\} \subset \Omega$, and the material distribution, $\mathbf{C}(\mathbf{X})$, such that an objective, $J(\omega, \mathbf{u})$, is extremized, constraints,

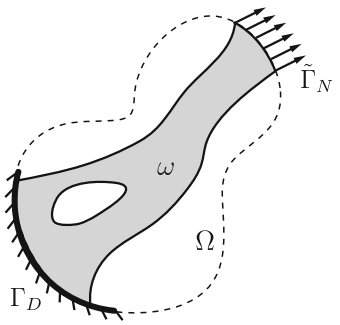

Fig. 3. Topology optimization problem schematic (notation follows Talischi et al. [43]).

$g_j(\omega, \mathbf{u}) \leq 0$ $(j = 1, \ldots, N_c)$, are satisfied, and the displacement field, $\mathbf{u} \in U$, satisfies the governing elastostatics equation, written in weak form here:

$$\int_{\omega} \mathbf{C}(\mathbf{X}) \nabla \mathbf{u} \, : \nabla \delta \mathbf{u} \, d\mathbf{X} = \int_{\tilde{\Gamma}_N} \mathbf{t} \cdot \delta \mathbf{u} \, ds, \qquad \forall \delta \mathbf{u} \in U_o \tag{3}$$

where Ω is a set of material points, $\mathbf{X}$, in spatial dimension n_d with boundary $\partial\Omega$, $\omega \subset \Omega$ defines the optimal shape, $\mathbf{C}(\mathbf{X})$ is the spatially varying material tensor, $U = \{\mathbf{u} \in H^1 : \mathbf{u} = \bar{\mathbf{u}} \text{ on } \Gamma_D\}$ is the set of kinematically admissible displacements (trial functions), $U_o = \{\delta\mathbf{u} \in H^1 : \delta\mathbf{u} = 0 \text{ on } \Gamma_D\}$ is the set of test functions, Γ_D and Γ_N form a partition of $\partial\Omega$ with displacements, $\mathbf{u} = \bar{\mathbf{u}}$, prescribed on Γ_D and nonzero tractions, $\mathbf{t} = \bar{\mathbf{t}}$, prescribed on $\tilde{\Gamma}_N \subseteq \Gamma_N$. The scenario described above is shown in Fig. 3, with notation following that of Talischi et al. [43].

The optimal set of material points ω can be defined by indicator function χ such that:

$$\chi(\mathbf{X}) = \begin{cases} 1 & \text{if } \mathbf{X} \in \omega \\ 0 & \text{if } \mathbf{X} \in \Omega \setminus \omega \end{cases} \tag{4}$$

and the material distribution $\mathbf{C}(\mathbf{X})$ can be defined by selecting from a finite set of m material tensors at each material point such that:

$$\mathbf{C}(\mathbf{X}) = \mathcal{A}(S(\mathbf{X})) \tag{5}$$

where $S(\mathbf{X}) = \{\mathbf{C}_1, \ldots, \mathbf{C}_m\}$ is the set of material tensors for the m candidate materials at point $\mathbf{X}$ and $\mathcal{A}$ is a choice function for which $\mathcal{A}(S(\mathbf{X})) \in S(\mathbf{X})$ holds. With these definitions, the weak form of the governing elastostatics equation can be re-written over the entire domain, Ω, as:

$$\int_{\Omega} \chi(\mathbf{X}) \mathcal{A}(S(\mathbf{X})) \nabla \mathbf{u} \, : \nabla \delta \mathbf{u} \, d\mathbf{X} = \int_{\tilde{\Gamma}_N} \mathbf{t} \cdot \delta \mathbf{u} \, ds, \qquad \forall \delta \mathbf{u} \in U_o. \tag{6}$$

As posed, finding ω and $\mathbf{C}(\mathbf{X})$ becomes a large integer programming problem, which can be impractical to solve. Thus, the indicator function, χ, and choice function, $\mathcal{A}$, are re-cast as m continuous scalar fields, $\rho_i(\mathbf{X}) \in [0, 1]$, $i = 1, \ldots, m$, each representing the density distribution of each of the m candidate materials in Ω. The total density at $\mathbf{X}$ is then $\rho_T(\mathbf{X}) = \sum_{i=1}^{m} \rho_i(\mathbf{X})$. The magnitude of these density fields can be used to determine the contribution of the m candidate materials at point $\mathbf{X}$ according to an interpolation function, $\eta(\rho_1(\mathbf{X}), \ldots, \rho_m(\mathbf{X}), S(\mathbf{X}))$. The interpolation function may also serve to penalize intermediate densities so that $\rho_i(\mathbf{X})$ better approximates the integer problem [12,13,44] and to penalize material mixing.

As noted by, e.g., Bourdin [45], the problem pursued here is ill-posed in that a non-convergent sequence of solutions consisting of designs with increasingly fine perforations arises. In order to ensure existence of solutions and to enforce a minimum length scale, the density fields are filtered by convolution with a smoothing filter, F [45]:

$$\hat{\rho}_i(\mathbf{X}) = (F * \rho_i)(\mathbf{X}) = \int_{\Omega} F(\mathbf{X}, \mathbf{Y}) \rho_i(\mathbf{Y}) \, d\mathbf{Y} \tag{7}$$

where $\hat{\rho}_i(\mathbf{X})$ is the filtered density field of material i and the (linear) kernel filter is defined as:

$$F(\mathbf{X},\mathbf{Y}) = c(\mathbf{X}) \max\left(0, 1 - \frac{|\mathbf{X}-\mathbf{Y}|}{R}\right) \tag{8}$$

where R is the filter radius and $c(\mathbf{X})$ is a normalizing coefficient that ensures $\int_\Omega F(\mathbf{X},\mathbf{Y})\, d\mathbf{Y} = 1$. Finally, the material interpolation function can be re-written in terms of the filtered density fields such that the governing elastostatics equation becomes:

$$\int_\Omega \eta\left(\hat{\rho}_1(\mathbf{X}), \ldots, \hat{\rho}_m(\mathbf{X}), S(\mathbf{X})\right) \nabla\mathbf{u} \,:\nabla\delta\mathbf{u}\, d\mathbf{X} = \int_{\tilde{\Gamma}_N} \mathbf{t}\cdot\delta\mathbf{u}\, ds, \qquad \forall\delta\mathbf{u}\in U_o. \tag{9}$$

3.1. Discretization of the elastostatics problem

The solution to (9) can be approximated via the finite element method. The domain is discretized into finite elements with characteristic mesh size h. The trial and test functions on this discretization, $\mathbf{u}^h$ and $\delta\mathbf{u}^h$, are approximated using interpolation (shape) functions, N_j, such that, for example, the components of $\mathbf{u}^h$ are assembled from the nodal displacements of each element, $u_i^h = \sum_{j=1}^{n_n} N_j u_i\left(X_j\right)$, $i = 1,\ldots,n_d$, where n_n is the number of nodes per element. With this approximation of the displacement field, the governing equation written in discrete form becomes $\mathbf{Ku} = \mathbf{f}$, where the i,j term of the stiffness matrix, $\mathbf{K}$, is:

$$K_{ij} = \int_\Omega \eta\left(\hat{\rho}_1(\mathbf{X}), \ldots, \hat{\rho}_m(\mathbf{X}), S(\mathbf{X})\right) \nabla N_i \,:\nabla N_j\, d\mathbf{X} \tag{10}$$

and the external force applied at degree of freedom i is $f_i = \int_{\tilde{\Gamma}_N} \mathbf{t}\cdot N_i\, ds$.

3.2. Discretization of the optimization space

The density fields, $\rho_i(\mathbf{X}), i = 1,\ldots,m$, are described by a finite number of points that are defined, for convenience, in accordance with the finite element discretization at the element level (see e.g., [43,46]). The discretized design variables, denoted z_i^e, $i = 1,\ldots,m$, $e = 1,\ldots,N$, represent the density of material i in element e, where m is the number of candidate materials available in the domain and N is the number of elements in the domain.

As discussed in Section 3, in order to ensure existence of solutions, enforce a minimum length scale, and also to avoid numerical artifacts that may result from discretization (e.g., checkerboard patterns), the linear kernel filter provided in (8) is applied to each of the m density fields such that the discrete filtered density of material i in element e becomes $\hat{z}_i^e = \sum_j H_{ej} z_i^j$, with the weights of filter matrix, $\mathbf{H}$, defined as:

$$H_{ej} = \frac{F_{ej} V^j}{\sum_{l\in\mathcal{N}_e} F_{el} V^l} \tag{11}$$

In (11), the norm used to define F_{ej} (see (8)) is the Euclidean distance between design variables z_i^j and z_i^e and $\mathcal{N}_e = \{z_i^j : d(j,e) \le R\}$ is the neighborhood of element e [45]. The total volume, V_T^e, and total density, ρ_T^e, of material in element e are calculated as linear functions of the filtered element densities, i.e., $V_T^e = \sum_{i=1}^m \hat{z}_i^e V^e$ and $\rho_T^e = \sum_{i=1}^m \hat{z}_i^e$.

3.3. Material interpolation

As in two-phase topology optimization, a penalization model is used to push the continuous design variables to their bounds. Two commonly used approaches are SIMP [12,13] and RAMP (Rational Approximation of Material Properties, [44]). Similarly, in the case of up to m candidate materials, penalized element densities for each candidate material are defined as $\tilde{z}_i^e\left(\hat{z}_i^e\right) = \left(\hat{z}_i^e\right)^p$ for SIMP or $\tilde{z}_i^e\left(\hat{z}_i^e\right) = \hat{z}_i^e / \left(1 + q\left(1-\hat{z}_i^e\right)\right)$ for RAMP, where $p > 1$ and $q > 0$ are penalty constants that help push the densities of each material toward zero and one.

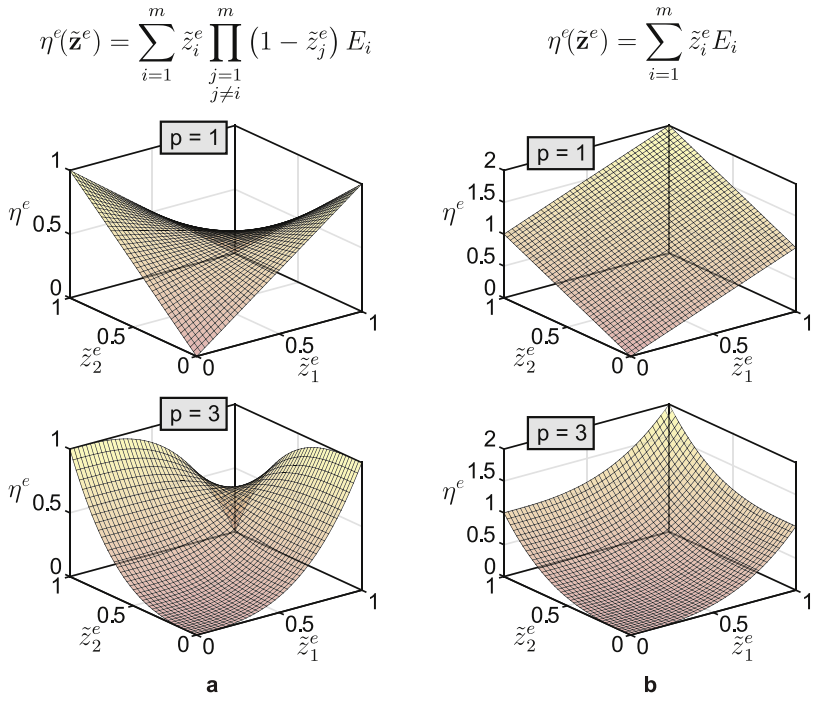

Fig. 4. Material interpolation function, η^e, in element e with $E_i = 1 \quad \forall i$ and using (a) the weights defined in (13); and (b) weights, $w_i^e\left(\tilde{\mathbf{z}}^e\right) = \tilde{z}_i^e$. Two candidate materials and the SIMP penalty function with $p = 1$ and $p = 3$ are considered.

For material selection, the penalized densities are coupled with a material interpolation scheme adopted from the DMO techniques [20,22], which are characterized by a summation of weighted material properties:

$$\eta^e\left(\tilde{\mathbf{z}}^e\right) = \sum_{i=1}^{m} w_i^e\left(\tilde{\mathbf{z}}^e\right) E_i, \quad e = 1, \ldots, N \tag{12}$$

where $w_i^e\left(\tilde{\mathbf{z}}^e\right)$ is the weight of material i in element e and E_i is the modulus of elasticity associated with material i. The goal during the optimization is to find values of the design variables such that a single material weight is active in each element (i.e., $w_i^e = 1$ and $w_{j\neq i}^e = 0, \quad \forall e$). In pursuit of this goal, the following weights, proposed by Stegmann and Lund [20], are considered:

$$w_i^e\left(\tilde{\mathbf{z}}^e\right) = \tilde{z}_i^e \prod_{\substack{j=1 \\ j\neq i}}^{m} \left(1-\tilde{z}_j^e\right), \quad i = 1, \ldots, m, \quad e = 1, \ldots, N. \tag{13}$$

As expected, in the case of a single solid phase, $w_i^e\left(\tilde{\mathbf{z}}^e\right) = \tilde{z}_i^e$, and the material interpolation corresponding to either SIMP or RAMP for two-phase topology optimization is recovered. Note that voids appear when the element densities are zero, i.e., void is not explicitly provided as a candidate material in the present formulation.

The material interpolation function, η^e, in element e is visualized in Fig. 4(a) for a two-material case considering the SIMP penalty function with $p = 1$ and $p = 3$ ($E_i = 1 \quad \forall i$ for demonstration purposes). Note that for both values of p, the material interpolation function goes to zero when both materials have density equal to one, i.e., material mixing is unfavorable. Additionally, increased p makes intermediate densities less efficient. As a result, the presence of both material mixing and intermediate densities is reduced with use of the weights in (13).

The effect of the product term in (13) becomes more apparent by comparing the material interpolation function using the weights in (13) to the case when $w_i^e\left(\tilde{\mathbf{z}}^e\right) = \tilde{z}_i^e$ as shown in Fig. 4(b), i.e., when the product term in (13) is neglected. Notice that without the product term, the interpolation is a linear function for $p = 1$ and neither

intermediate densities nor material mixing are penalized; in fact, material mixing may be favored as it amplifies the element stiffness. As p is increased to 3, intermediate densities become less efficient, but material mixing may still be favored. Other weighting schemes have been considered; for example, Bruyneel [47] specifies the weights using finite element shape functions.

3.4. Sensitivity analysis

The sensitivity of compliance can be evaluated via the chain rule as follows:

$$\frac{\partial J}{\partial z_i^e} = \frac{\partial J}{\partial \eta^e}\frac{\partial \eta^e}{\partial \tilde{z}_j^k}\frac{\partial \tilde{z}_j^k}{\partial \hat{z}_l^r}\frac{\partial \hat{z}_l^r}{\partial z_i^e}, \quad i = 1, \ldots, m, \quad e = 1, \ldots, N \tag{14}$$

where the derivative of compliance with respect to the interpolated stiffness has been derived as (see e.g., [48]):

$$\frac{\partial J}{\partial \eta^e} = -\mathbf{u}^e\left(\mathbf{z}_1, \ldots, \mathbf{z}_m\right)^T \frac{\partial \mathbf{k}^e}{\partial \eta^e}\mathbf{u}^e\left(\mathbf{z}_1, \ldots, \mathbf{z}_m\right), \quad e = 1, \ldots, N \tag{15}$$

Note that the stiffness matrix of element e, $\mathbf{k}^e$, can be expressed as a constant matrix, $\mathbf{k}_o^e$, multiplied by the material interpolation function, η^e:

$$\mathbf{k}^e = \left[E_{min} + (1 - E_{min})\eta^e\left(\tilde{\mathbf{z}}^e\right)\right]\mathbf{k}_o^e \tag{16}$$

where E_{min} is an Ersatz stiffness used to avoid singularities in the stiffness matrix. Then, the derivative of the element stiffness matrix with respect to the interpolated stiffness in element e is:

$$\frac{\partial \mathbf{k}^e}{\partial \eta^e} = (1 - E_{min})\,\mathbf{k}_o^e. \tag{17}$$

The remaining terms in (14) are computed as follows. The derivative of the material interpolation function is:

$$\frac{\partial \eta^e\left(\tilde{\mathbf{z}}^e\right)}{\partial \tilde{z}_j^k} = \begin{cases} \prod_{\substack{i=1\\ i\neq j}}^{m}\left(1 - \tilde{z}_i^k\right)E_j - \sum_{\substack{l=1\\ l\neq j}}^{m}\tilde{z}_l^k\prod_{\substack{r=1\\ r\neq l\\ r\neq j}}^{m}\left(1 - \tilde{z}_r^k\right)E_l & \text{if} \quad k = e \\ 0 & \text{otherwise,} \end{cases} \tag{18}$$

the derivative of the penalized density is:

$$\frac{\partial \tilde{z}_j^k}{\partial \hat{z}_l^r} = \begin{cases} p\left(\hat{z}_l^r\right)^{p-1} & \text{(SIMP)} \quad \text{if} \quad r = k \quad \text{and} \quad l = j \\ \dfrac{q+1}{\left[1 + q\left(1 - \hat{z}_l^r\right)\right]^2} & \text{(RAMP)} \quad \text{if} \quad r = k \quad \text{and} \quad l = j \\ 0 & \text{otherwise,} \end{cases} \tag{19}$$

and the derivative of the filtered density is:

$$\frac{\partial \hat{z}_l^r}{\partial z_i^e} = \begin{cases} H_{re} & \text{if} \quad i = l \\ 0 & \text{otherwise.} \end{cases} \tag{20}$$

Note that the derivative of η^e in (18) may be non-positive in regions in which mixing occurs, causing (14) to become non-negative, and leading to inconsistencies in the ZPR design variable update (see the clearly non-monotonous plots of η^e in Fig. 4(a)). However, these mixing regions are small and localized as shown in Section 6.2.2, and neglecting the sensitivities of the design variables in those regions does not prevent the formulation from yielding reasonable results (both qualitatively and quantitatively). Non-negative sensitivities have been treated in this way for compliant mechanism design [49].

The derivatives of the linear volume/mass constraints are:

$$\frac{\partial g_j}{\partial z_i^e} = \frac{\partial g_j}{\hat{z}_l^r}\frac{\hat{z}_l^r}{\partial z_i^e}, \quad \frac{\partial g_j}{\hat{z}_l^r} = \gamma_l V^r, \quad j = 1, \ldots, N_c, \quad i = 1, \ldots, m, \quad e = 1, \ldots, N. \tag{21}$$

4. The ZPR design variable update in the continuum setting

The Optimality Criteria (OC) design variable update is widely used for volume constrained compliance minimization problems in two-phase topology optimization because of its simplicity and applicability to problems in which an increase in the quantity associated with the constraint leads strictly to a reduction in the objective. In general, the OC method can only accommodate a single volume constraint, which has led to the use of more complex update schemes, e.g., MMA [50], for multi-material topology optimization problems that consider multiple volume constraints [2,20,22]. However, by studying the primal–dual relationship of the linearized version of (1), it has been shown that the design variables associated with each constraint are independent of the other constraints and can be updated via sequential (or parallel) updates for each constraint, i.e., the ZPR update scheme [1]. The key to the validity of this approach is that the Lagrangian is a separable function of the Lagrange multipliers, which in turn requires that the constraints are variable separable.

The ZPR update is a sequential linear programming technique tailored to the volume constrained compliance minimization problem through intervening variables in the form of $y_i^e\left(z_i^e\right) = \left(z_i^e\right)^{-\alpha}, \quad \alpha > 0$. With these intervening variables, linearized approximations to (1) are solved using Lagrangian duality at each optimization step. The primal–dual relationship for problems with a single volume constraint (OC method) has been given, for example, by Christensen and Klarbring [48] and Groenwold and Etman [51]; and for multiple volume constraints (ZPR method) by Zhang et al. [1]. The resulting explicit update for material i in element e at iteration $(t+1)$ is given by:

$$z_i^e(\lambda_j) = z_i^{e,(t)} \left(-\frac{\left.\frac{\partial J}{\partial z_i^e}\right|_{z_i^e = z_i^{e,(t)}}}{\lambda_j \left.\frac{\partial g_j}{\partial z_i^e}\right|_{z_i^e = z_i^{e,(t)}}} \right)^{\frac{1}{1+\alpha}} =: B_i^e(\lambda_j). \tag{22}$$

Note that the update of each design variable is dependent only on the Lagrange multiplier, λ_j, of the constraint to which it is associated [1]. To achieve improved results for continuum problems with many materials, the filter is applied during the update so that the update of material i in element e becomes $z_i^e(\lambda_j) = \sum_k H_{ek} B_i^k\left(\lambda_j\right)$. It is emphasized that this modification to the ZPR update scheme [1] is heuristic, but is found to lead to improved results for continuum problems.

Design changes in (22) are controlled and kept within the box constraints using lower and upper bounds, $\underline{z}_i^e$ and $\overline{z}_i^e$, respectively:

$$z_i^e(\lambda_j) = \begin{cases} \underline{z}_i^e & \text{if} \quad \sum_k H_{ek} B_i^k(\lambda_j) \le \underline{z}_i^e \\ \sum_k H_{ek} B_i^k(\lambda_j) & \text{if} \quad \underline{z}_i^e \le \sum_k H_{ek} B_i^k(\lambda_j) \le \overline{z}_i^e \\ \overline{z}_i^e & \text{if} \quad \sum_k H_{ek} B_i^e(\lambda_j) \ge \overline{z}_i^e \end{cases} \tag{23}$$

where the bounds are defined by the move limit, δ:

$$\underline{z}_i^e = \max \begin{cases} z_i^e - \delta \\ 0 \end{cases} \qquad \overline{z}_i^e = \min \begin{cases} z_i^e + \delta \\ 1 \end{cases} \tag{24}$$

5. Implementation

In this section, some implementation details related to the ZPR update scheme and design post-processing are described. Two post-processing rules are described, which are heuristic techniques to the problem. Thus, other alternatives are possible depending on the immediate target.

5.1. ZPR design variable update

Since each design variable is dependent only on the Lagrange multiplier of the constraint it is associated with (refer to Section 4 and (22)), *the design variables can be updated one constraint at a time in an arbitrary order*. As such,

a loop is implemented over the design variable update scheme such that it is called N_c times, each time only passing the design variables and associated sensitivities corresponding to constraint j. Algorithm 1 provides the pseudo-code for the ZPR design variable update considering multiple volume/mass constraints for the case of a serial update [1]. However, because the constraints are independent, each update performed in the for-loop could be executed in parallel to increase efficiency.

Algorithm 1 ZPR design variable update implemented sequentially

```
for j = 1 to N_c do
    Initialize bisection interval lower bound, λ_j^l
    Initialize bisection interval upper bound, λ_j^u
    while (λ_j^u − λ_j^l) / (λ_j^u + λ_j^l) > tolerance do
        update Lagrange multiplier λ_j of constraint j (bisection)
        update design variables z_i^e(λ_j) associated with constraint j (Eq. 23)
        if derivative of j^th term of the dual problem > 0 then
            reset interval lower bound, λ_j^l = λ_j
        else
            reset interval upper bound, λ_j^u = λ_j
        end if
    end while
end for
```

5.2. Design post-processing

The formulation in (1) is characterized by up to m design variables in each element, each representing the density, $z_i^e \in [0, 1]$, of one of the candidate materials. The goal is to find a design in which at most one of the design variables in each element has value equal to one and the others have zero value. The penalty function serves to push each individual design variable toward zero or one, but does not prevent multiple design variables in a given element from having value simultaneously (see Fig. 4(b)). To constrain the total density in each element (e.g., $\sum_{i=1}^{m} z_i^e \leq 1 \ \ \forall k$), as done by Hvejsel and Lund [23] and Hvejsel et al. [24], makes the optimization problem more complex and is not considered here. Instead, a simple post-processing step is found to be effective. Below two heuristic alternatives are discussed.

The DMO material interpolation defined in (12) and (13) penalizes material mixing (recall Fig. 4(a)). As noted by Gao and Zhang [2], when any of the weights, w_i^e, in (13) is exactly equal to one, all other weights must be zero. Thus, in the case that the penalty function is able to push the design variables exactly to their 0/1 bounds, the final design corresponds to a discrete 0/1 design without any mixing. However, due to the density filter, intermediate densities appear at material boundaries, leading to mixing at material interfaces and total element densities (i.e., $\rho_T^e = \sum_{i=1}^{m} \hat{z}_i^e$) possibly greater than one.

To remove cases in which total density is greater than one in a given element and/or to completely remove mixing from the design, two post-processing techniques are considered:

Heuristic post-processing technique # 1:
In each element that contains multiple materials, assign a density equal to $\min\left\{\rho_T^e, 1\right\}$ to the design variable associated with the material that has the largest contribution to ρ_T^e and assign a density of zero to the design variables associated with all other materials. Break ties by selecting the stiffer of materials with the same contribution to ρ_T^e. *This approach removes all mixing and non-physical situations in which* $\rho_T^e > 1$.

Heuristic post-processing technique # 2:
For each element that contains multiple materials and $\rho_T^e > 1$, scale the contribution of each material such that the total element density is equal to one and the relative contributions of the materials remain unchanged. *This approach does not eliminate mixing, but removes non-physical situations in which* $\rho_T^e > 1$.

Since post-processing technique #2 proportionally scales back the contribution of each material to avoid total densities greater than one, it is expected to cause the objective to increase (stiffness is reduced) and guarantees that the

Table 1
Brief description of the multi-material numerical examples.

Example	Dimension	Description	Remarks
1	2D	Tension member	• Global and local volume constraints are explored with many materials • Solutions are obvious for a human-being, but not for a computer
2	2D	Bending member (MBB beam)	• Material distributions agree with mechanics principles • Heuristic post-processing techniques have little impact on behavior • Single global mass constraint yields multi-material design
3	2D	Local volume constraints	• Lots of volume constraints lead to designs with controlled porosity • Local volume constraints may serve as a microstructure design tool
4	3D	Cantilever beam	• Topology optimization and additive manufacturing are connected

volume constraints will remain satisfied. In contrast, it is not clear whether the objective will increase or decrease after applying post-processing technique #1 or what the effect on the volume constraints will be. However, the objective may tend to reduce as a result of applying post-processing technique #1 since it eliminates mixing; recall that elements with material mixing tend to be less stiff according to the material interpolation scheme (see Fig. 4(a)). Additionally, since mixing tends to result from filtering and is typically limited to the intersection of materials (i.e., addition and removal of material across a material boundary will tend to cancel out), it is anticipated that the volume constraints will also reduce with post-processing technique #1 (note that the total volume of material is guaranteed to reduce as total densities greater than one are removed). A comparison of the compliance, volume fractions, and total element densities before and after post-processing (techniques #1 and #2) are provided in Section 6.2.2 and it is shown that, for the considered problems, the effect of post-processing on the global mechanical behavior (compliance) is minor and the constraints remain satisfied after post-processing.

6. Examples

Four numerical examples based on a MATLAB implementation demonstrate the key features, capabilities, and limitations of the present formulation for multi-material topology optimization. A summary of the examples is provided in Table 1.

All candidate materials are fully dense and without associated costs ($\gamma_i = 1 \ \ \forall i$), unless stated otherwise, and are linear elastic and isotropic, i.e., they are defined by two scalar parameters: modulus of elasticity, E_i, and Poisson's ratio, ν_i, for material i. All examples consider the SIMP penalty function and an Ersatz stiffness of $E_{min} = 1 \times 10^{-9}$. Additional optimization parameters considered for each example are provided in Table 2. The specified convergence tolerance defines the acceptable magnitude of change in design variables (infinity norm) used as a stopping criterion for the optimization algorithm. It is also noted that the formulation performs best when the initial guess does not favor any one candidate material. Thus, in all examples, the initial guess is specified such that all of the elements controlled by a given constraint have an equal initial density of each candidate material and the volume/mass constraint is satisfied in equality (or very close to equality for the mass constrained problem).[1]

6.1. 2D tension member

A tension member is studied to demonstrate that the proposed approach is effective in accommodating many materials and that the algorithm is able to achieve solutions that seem obvious to a human-being, but that are not

[1] Unless otherwise noted, the plots provided for all of the 2D results are surface plots with the x- and y-axes in the plane of the design and the z-axis representing the filtered density of each material (i.e., results are plotted with some finite thickness). For the 2D results, intermediate densities below 0.3 are not plotted. The 2-material 3D result is shown as a single isosurface with color indicating the two filtered density fields of the two materials. The 3D plotting routine is based on that developed by Zegard and Paulino [7] for single material designs, but has been modified for multi-material. Intermediate densities below 0.5 are not plotted for the 3D results.

Table 2
Optimization parameters used for all examples.

	2D	3D
SIMP penalty parameter, p	3	*continuation* [1 → 3]
Filter radius, R	2	4
OC move limit, δ	0.2	0.15
OC linearization exponent, α	2	2
Convergence tolerance	0.008	0.01

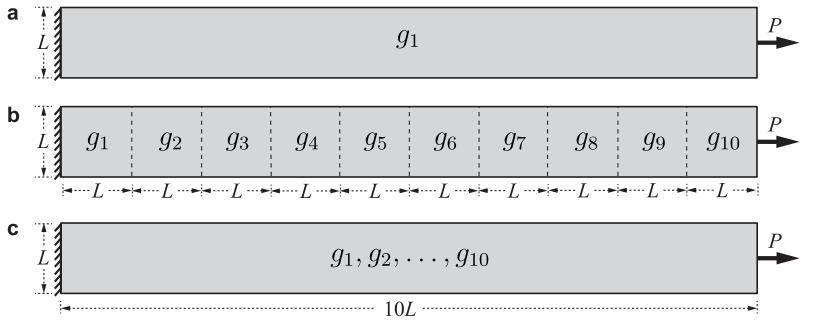

Fig. 5. Tension member domain and boundary conditions with (a) one constraint controlling the entire domain (i.e., a global constraint); (b) ten constraints controlling ten sub-regions of the domain (i.e., local constraints); and (c) ten constraints each controlling the entire domain.

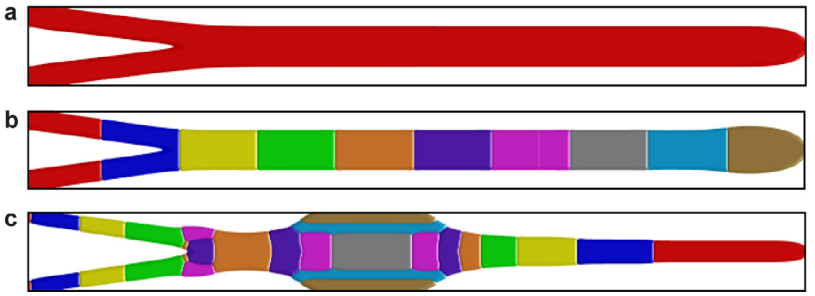

Fig. 6. Tension member designs for (a) a single volume constraint controlling all ten candidate materials in the entire domain (i.e., a global constraint); (b) ten volume constraints controlling a subset of the ten candidate materials in ten sub-regions of the domain (i.e., local constraints); and (c) ten volume constraints, each controlling a single candidate material in the entire domain (color online).

straightforward for a computer to obtain. The domain and boundary conditions for the tension member, as well as sub-regions controlled by the indicated volume constraints, are shown in Fig. 5, where the length parameter L is taken to be 60 and P is a unit load. In all three cases, the domain is discretized into a 600×60 orthogonal finite element mesh composed of four-node quadrilateral elements. Material properties for ten candidate materials considered for design of the tension member are provided along with their associated constraints in Tables 3–5 for the three considered cases.

First, a single volume constraint is specified to limit all ten candidate materials to fill no more than 50% of the entire domain volume (see Fig. 5(a) and Table 3). Since all candidate materials are linear elastic and isotropic, the expected solution for compliance minimization is a two-phase design in which the only non-void phase that shows up in the design is the one with largest modulus of elasticity. The resulting design, which is in agreement with intuition, is provided in Fig. 6(a).

Next, ten volume constraints are specified such that each limits a subset of the ten candidate materials to fill no more than 50% of a sub-region of the domain. The sub-regions controlled by each constraint are shown in Fig. 5(b) and the candidate materials associated with each constraint are summarized in Table 4. The first constraint controls all ten of the candidate materials, the second constraint controls all but the stiffest candidate material, the third constraint

Table 3
Candidate materials associated with the volume constraint for the problem depicted in Fig. 5(a) considering Poisson's ratio $\nu_i = 0.3$ (constant), $i = 1, \ldots, 10$.

Mat.	E_i	Constraint g_1
1	1	✓
2	0.9	✓
3	0.8	✓
4	0.7	✓
5	0.6	✓
6	0.5	✓
7	0.4	✓
8	0.3	✓
9	0.2	✓
10	0.1	✓
Volume fraction:		$\frac{1}{2}$

Table 4
Candidate materials associated with each of the ten volume constraints for the problem depicted in Fig. 5(b) considering Poisson's ratio $\nu_i = 0.3$ (constant), $i = 1, \ldots, 10$.

Mat.	E_i	Constraints									
		g_1	g_2	g_3	g_4	g_5	g_6	g_7	g_8	g_9	g_{10}
1	1	✓	–	–	–	–	–	–	–	–	–
2	0.9	✓	✓	–	–	–	–	–	–	–	–
3	0.8	✓	✓	✓	–	–	–	–	–	–	–
4	0.7	✓	✓	✓	✓	–	–	–	–	–	–
5	0.6	✓	✓	✓	✓	✓	–	–	–	–	–
6	0.5	✓	✓	✓	✓	✓	✓	–	–	–	–
7	0.4	✓	✓	✓	✓	✓	✓	✓	–	–	–
8	0.3	✓	✓	✓	✓	✓	✓	✓	✓	–	–
9	0.2	✓	✓	✓	✓	✓	✓	✓	✓	✓	–
10	0.1	✓	✓	✓	✓	✓	✓	✓	✓	✓	✓
Volume fraction:		$\frac{1}{2}$	$\frac{1}{2}$	$\frac{1}{2}$	$\frac{1}{2}$	$\frac{1}{2}$	$\frac{1}{2}$	$\frac{1}{2}$	$\frac{1}{2}$	$\frac{1}{2}$	$\frac{1}{2}$

controls all but the two stiffest candidate materials, and so on. Using the same logic as in the previous example, it is expected that the only material that will appear in each sub-region is that with the largest modulus of elasticity. The corresponding solution is provided in Fig. 6(b) and agrees well with human intuition, but it is somewhat surprising that the algorithm could obtain such a predictably clean solution.

Lastly, ten volume constraints are specified such that each limits a single candidate material to fill no more than 5% of the entire domain volume (see Fig. 5(c) and Table 5). If all ten materials are used to their limits, the domain will be 50% filled with material. Here, the solution is not as obvious, even to a human, but the resulting design in Fig. 6(c) is a valid one. The final design captures the local effects of the boundary conditions by distributing the stiffest materials to the regions with loading and support conditions and distributing vertical layers of decreasingly stiff materials inward from both ends. Additionally, the tension member is thinner in regions where the stiffer materials are distributed and thicker toward the center, where the least stiff materials are layered horizontally above and below the main structure.

6.2. 2D MBB beam

The MBB beam is used to demonstrate that:

1. the formulation leads to material distributions that qualitatively agree with principles of mechanics for a bending problem;

Table 5
Candidate materials associated with each of the ten volume constraints for the problem depicted in Fig. 5(c) considering Poisson's ratio $\nu_i = 0.3$ (constant), $i = 1, \ldots, 10$.

Mat.	E_i	Constraints									
		g_1	g_2	g_3	g_4	g_5	g_6	g_7	g_8	g_9	g_{10}
1	1	✓	–	–	–	–	–	–	–	–	–
2	0.9	–	✓	–	–	–	–	–	–	–	–
3	0.8	–	–	✓	–	–	–	–	–	–	–
4	0.7	–	–	–	✓	–	–	–	–	–	–
5	0.6	–	–	–	–	✓	–	–	–	–	–
6	0.5	–	–	–	–	–	✓	–	–	–	–
7	0.4	–	–	–	–	–	–	✓	–	–	–
8	0.3	–	–	–	–	–	–	–	✓	–	–
9	0.2	–	–	–	–	–	–	–	–	✓	–
10	0.1	–	–	–	–	–	–	–	–	–	✓
Volume fraction:		$\frac{1}{20}$	$\frac{1}{20}$	$\frac{1}{20}$	$\frac{1}{20}$	$\frac{1}{20}$	$\frac{1}{20}$	$\frac{1}{20}$	$\frac{1}{20}$	$\frac{1}{20}$	$\frac{1}{20}$

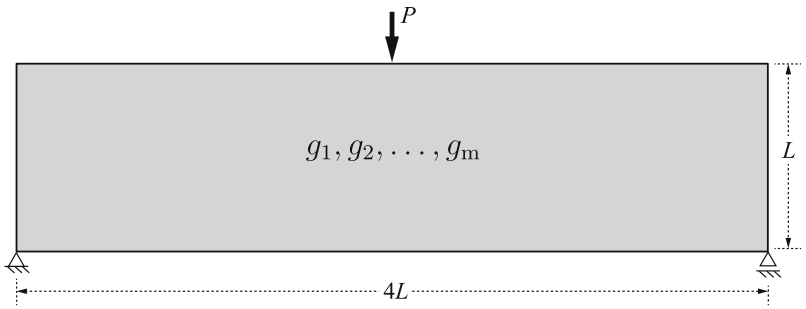

Fig. 7. MBB beam domain and boundary conditions with constraints shown to control the entire domain (only half of the domain is modeled and symmetry is assumed along the vertical centerline).

2. the post-processing techniques do not significantly impact the mechanical behavior of the design and do not lead to constraint violations for the problems considered;
3. the formulation is effective at achieving multi-material designs with specification of a single global mass constraint that controls multiple candidate materials in the entire domain by considering candidate materials with varying stiffness-to-mass ratios.

The domain and boundary conditions for the MBB beam are provided in Fig. 7 and the parameters considered are $L = 60$ and $P = 1$. Half of the domain is discretized into a 120×60 orthogonal finite element mesh composed of four-node quadrilateral elements. Symmetry along the vertical centerline of the domain is assumed and results are shown with symmetry imposed.

6.2.1. 2D MBB beam: Global volume constraints on individual materials

To demonstrate that the presented formulation is effective at distributing materials in accordance with basic principles of mechanics, the MBB beam is designed considering a volume constraint for each of two, three, four, and five of the candidate materials described in Table 6, in the entire domain. The parameter, V_j^{max}, is specified for each material according to the volume fractions provided in Table 6 such that the total allowable volume is 50% of the domain volume and is divided evenly between each of the candidate materials.

The converged results in Fig. 8 demonstrate that the presented formulation leads to results that agree with intuition from a mechanics perspective. In all cases, the stiffest material is distributed to the regions of the beam where stresses are expected to be highest and materials with reduced stiffness are distributed toward the neutral axis where stresses are expected to be low. In fact, in the four and five material designs (Fig. 8(c) and (d)), distinct horizontal "layers" of materials are observed: the least stiff materials are located toward the middle and the stiffest are toward the top

Table 6
Candidate materials and specified volume constraints for 2, 3, 4, and 5-material MBB beam designs considering Poisson's ratio $\nu_i = 0.3$ (constant), $i = 1, \ldots, 10$.

Mat.	E_i	2-material (Fig. 8(a))		3-material (Fig. 8(b))			4-material (Fig. 8(c))				5-material (Fig. 8(d))				
		g_1	g_2	g_1	g_2	g_3	g_1	g_2	g_3	g_4	g_1	g_2	g_3	g_4	g_5
1	1	✓	–	✓	–	–	✓	–	–	–	✓	–	–	–	–
2	0.8	–	–	–	–	–	–	✓	–	–	–	✓	–	–	–
3	0.5	–	✓	–	✓	–	–	–	–	–	–	–	✓	–	–
4	0.4	–	–	–	–	–	–	–	✓	–	–	–	–	✓	–
5	0.2	–	–	–	–	✓	–	–	–	✓	–	–	–	–	✓
Volume fraction:		$\frac{1}{4}$	$\frac{1}{4}$	$\frac{1}{6}$	$\frac{1}{6}$	$\frac{1}{6}$	$\frac{1}{8}$	$\frac{1}{8}$	$\frac{1}{8}$	$\frac{1}{8}$	$\frac{1}{10}$	$\frac{1}{10}$	$\frac{1}{10}$	$\frac{1}{10}$	$\frac{1}{10}$

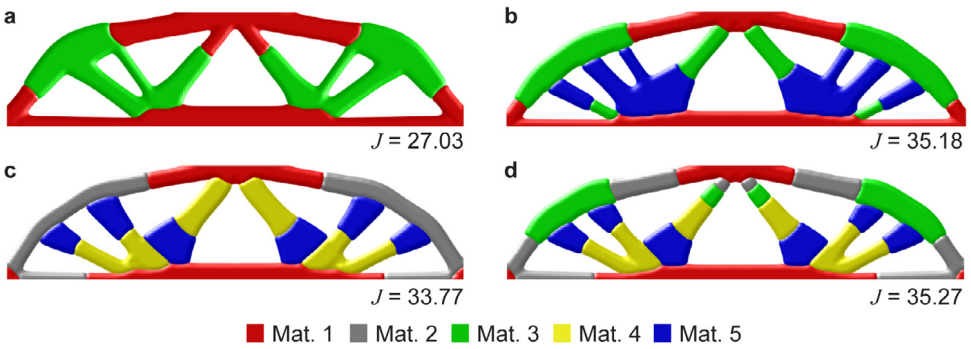

Fig. 8. Multi-material MBB beam designs with individual global volume constraints for each of (a) 2; (b) 3; (c) 4; and (d) 5 candidate materials. Plotted material distributions and objective values are based on the converged results (i.e., before post-processing) (color online).

Table 7
MBB beam: compliance of the converged and post-processed designs.

	2-material	3-material	4-material	5-material
At convergence	27.03	35.18	33.77	35.27
Post-processing technique #1	26.47	33.75	31.98	32.96
Post-processing technique #2	27.91	36.44	35.59	38.24

and bottom surfaces. The final objective value is listed beneath each design in Fig. 8 and the full convergence plot for each is provided in Fig. 9(a). A comparative investigation of the cases illustrated by Fig. 8 indicate that the different multi-material designs lead to different geometrical and topological configurations. In reference to the latter case, notice that the beams in Fig. 8(a), (b), and (d) have seven holes, while the beam in Fig. 8(c) has nine holes.

6.2.2. 2D MBB beam: Post-processing techniques

This example is also used to show the effect of the two post-processing techniques described in Section 5.2. For each of the four designs, the compliance and volume fractions of each candidate material are provided in Tables 7 and 8, respectively, for the results obtained at convergence and for those obtained after applying the two post-processing techniques. Note that, as predicted (see discussion in Section 5.2), post-processing technique #1 leads to minor reductions in the objective while post-processing technique #2 leads to minor increases in the objective. Both post-processing techniques lead to reductions in the volume fractions of each candidate material (i.e., no constraint violations). The observed trends are specific to the problem at hand and may not hold for other problems. Nevertheless, this study provides evidence that, although the formulation allows material mixing and possibly (non-physical) total

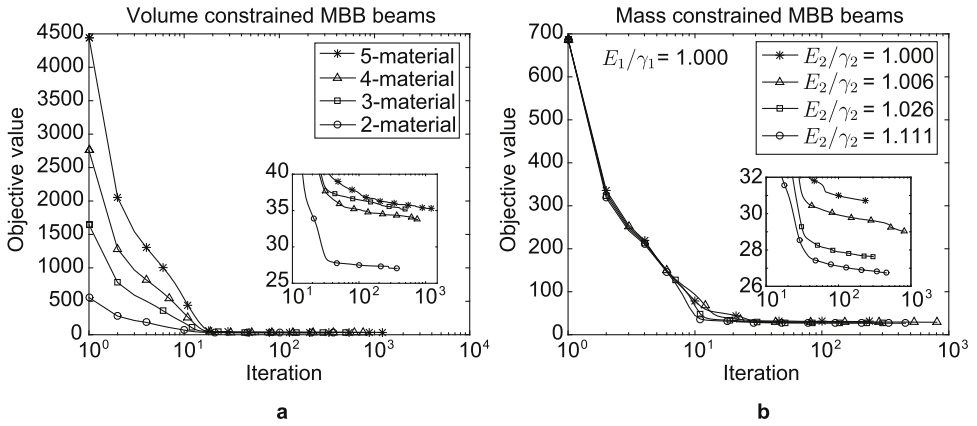

Fig. 9. Objective value vs. iteration for (a) multi-material MBB beams with individual global volume constraints for each of the candidate materials (refer to Section 6.2.1); and (b) 2-material MBB beams with a single global mass constraint and varying stiffness-to-mass ratios (refer to Section 6.2.3).

Table 8
MBB beam: volume fractions (in brackets) of the converged and post-processed designs (compare to the volume constraints listed in Table 6).

	2-material design [Mat. 1, Mat. 3]	4-material design [Mat. 1, Mat. 2, Mat. 4, Mat. 5]
At convergence	[0.2500, 0.2500]	[0.1250, 0.1250, 0.1250, 0.1250]
Post-processing technique #1	[0.2477, 0.2480]	[0.1238, 0.1240, 0.1209, 0.1233]
Post-processing technique #2	[0.2480, 0.2476]	[0.1234, 0.1239, 0.1223, 0.1223]
	3-material design [Mat. 1, Mat. 3, Mat. 4]	5-material design [Mat. 1, Mat. 2, Mat. 3, Mat. 4, Mat. 5]
At convergence	[0.1667, 0.1667, 0.1667]	[0.1000, 0.1000, 0.1000, 0.1000, 0.1000]
Post-processing technique #1	[0.1658, 0.1642, 0.1650]	[0.0997, 0.0976, 0.0980, 0.0963, 0.0971]
Post-processing technique #2	[0.1655, 0.1646, 0.1649]	[0.0984, 0.0978, 0.0979, 0.0974, 0.0972]

densities exceeding one, the converged results are realistic in that post-processing does not lead to significant changes in the global mechanical behavior or lead to constraint violations.

In Figs. 10 and 11, the 3-material MBB beam design is used to demonstrate that, although the formulation does not enforce strict constraints to avoid material mixing or total densities exceeding one, the material interpolation scheme is effective at avoiding this type of behavior throughout the majority of the design. Observation indicates that cases of material mixing and material densities exceeding one are typically limited to regions where distinct materials intersect. In Fig. 10, each of the three candidate material densities are mapped to intensities of red, green, and blue, for materials one, three, and five of Table 6, respectively, and plotted using the corresponding RGB values. Two views of the RGB mixing cube are provided in Fig. 10(a) for comparison with the mixing shown for the converged (Fig. 10(b)) and post-processed designs (Fig. 10(c) and (d) for techniques #1 and #2, respectively). Note that the standard RGB mixing cube has been rotated such that when all three materials are at their lower bounds, the intensities of red, green, and blue are equal to zero, resulting in white (absence of material). When all three materials are at their upper bounds, the intensities of red, green, and blue are equal to one, resulting in black (this case is avoided with the selected material interpolation scheme). Mixing is clearly limited to regions at which the materials intersect. Post-processing technique #1 removes all mixing and post-processing technique #2 does not, as expected. In Fig. 11(a), the total element densities, ρ_T^e, are plotted and it is observed that at convergence the total element densities exceed one at the intersection of distinct materials. Both post-processing techniques eliminate this anomaly, leading to almost identical plots of total element densities in both cases, as shown in Fig. 11(b) and (c).

6.2.3. 2D MBB beam: Single global mass constraint for 2-material design

For linear elastic, isotropic materials with a single volume constraint controlling all of the materials, the optimizer will always select the stiffest material for the minimum compliance problem (recall the result in Fig. 6a). In the

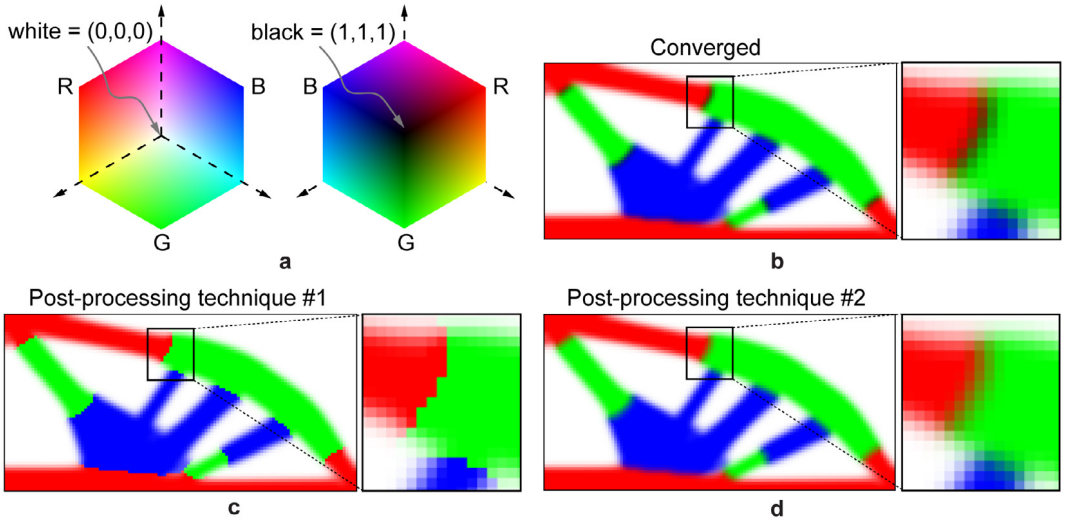

Fig. 10. Demonstration that material mixing may occur at the intersection of distinct material regions and the effect of post-processing on material mixing: (a) Two views of the RGB cube, which has been rotated so that white is at the origin to represent void. The rotated RGB cube is a reference for the mixing shown in the 3-material MBB beam (b) at convergence; (c) after post-processing (technique #1); and (d) after post-processing (technique #2), with densities of each material mapped to an RGB value. The density of material 1 represents the intensity of red, the density of material 3 represents the intensity of green, and the density of material 5 represents the intensity of blue. Absence of material is denoted by white and presence of all three materials (at their upper bounds) is denoted by black (color online).

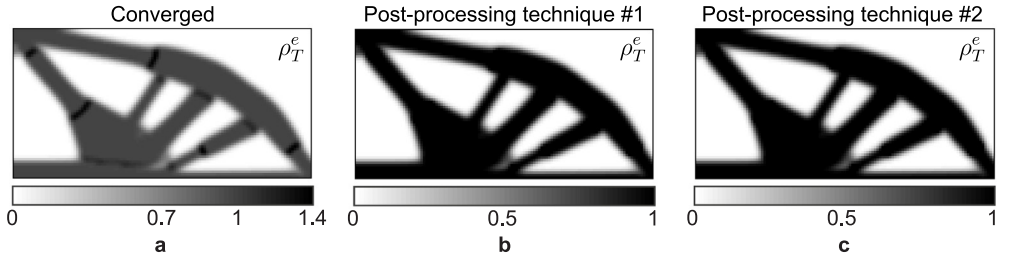

Fig. 11. Demonstration that total material densities may exceed one at the intersection of distinct material regions and the effect of post-processing on the total material densities: 3-material MBB beam (a) at convergence; (b) after post-processing technique #1; (c) after post-processing technique #2.

previous sub-section, multi-material designs were obtained by imposing separate volume constraints on each of the candidate materials, allowing all of the available materials to emerge and be used to their limits. In this sub-section, *scale factors*, γ_i, *are applied to the materials and it is shown that multi-material designs can be obtained even when all materials are controlled by a single global constraint*. By varying the stiffness-to-mass ratios of the candidate materials, the optimizer may select a less stiff material in favor of a less dense material [2–6]. Although not explicitly considered here, cellular materials may have varying stiffness-to-mass ratios and could be considered as candidate materials in the present formulation.

The MBB beam is designed with a global mass constraint considering the two candidate materials described in Table 9, i.e., $E_1 = 1$ and $E_2 = 0.5$. The mass density of material 1 is held constant ($\gamma_1 = 1$) and that of material 2 is varied ($\gamma_2 = 0.5, 0.49, 0.48, 0.47$ for cases a, b, c, and d, respectively). Thus, the stiffness-to-mass ratio of material 1 is $E_1/\gamma_1 = 1.000$, while that of material 2 is $E_2/\gamma_2 = 1.000, 1.020, 1.042, 1.064$ for cases a, b, c, and d, respectively. In all cases, the mass limit, $M^{max} = 0.35V^{total}$, where V^{total} is the total domain volume.

Table 9
Candidate materials associated with the global mass constraints for four cases of the problem depicted in Fig. 7 considering Poisson's ratio $\nu_i = 0.3$ (constant), $i = 1, \ldots, 10$.

Mat.	E_i	γ_i	$E_i\ \gamma_i$	Constraint			
				(Fig. 14(a))	(Fig. 14(b))	(Fig. 14(c))	(Fig. 14(d))
				g_1	g_1	g_1	g_1
1	1	1	1.000	✓	✓	✓	✓
2a	0.5	0.5	1.000	✓	–	–	–
2b	0.5	0.49	1.020	–	✓	–	–
2c	0.5	0.48	1.042	–	–	✓	–
2d	0.5	0.47	1.064	–	–	–	✓
M^{max}/V^{total}				0.35	0.35	0.35	0.35

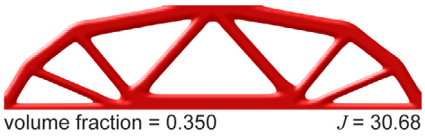

Fig. 12. Single material MBB beam design for material 1 ($E_1 = 1$, $\gamma_1 = 1$) (color online).

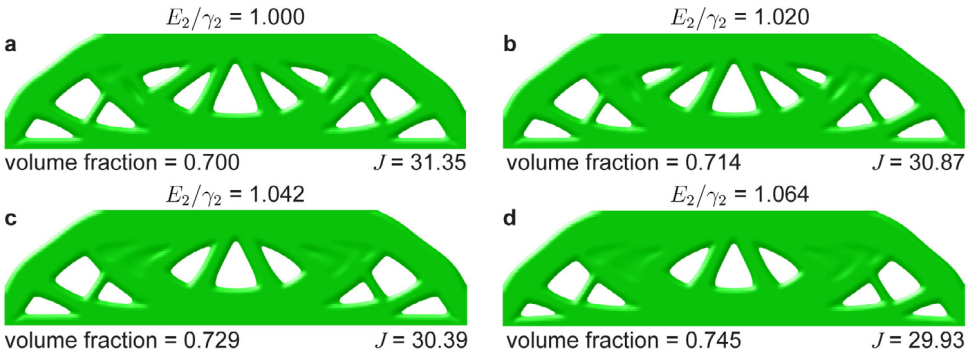

Fig. 13. Single material MBB beam design for materials: (a) 2a ($E_2 = 0.5$, $\gamma_1 = 0.5$); (b) 2b ($E_2 = 0.5$, $\gamma_1 = 0.49$); (c) 2c ($E_2 = 0.5$, $\gamma_1 = 0.48$); (d) 2d ($E_2 = 0.5$, $\gamma_1 = 0.47$) (color online).

First, a single material problem considering material 1 and four single-material problems considering materials 2a, 2b, 2c, and 2d (Table 9) are conducted to demonstrate that in a mass constrained problem, the stiffness, E_i, and mass density, γ_i, both influence the volume and compliance of the final design. According to the mass constraint, the allowable volume fraction of material i is equal to $0.35/\gamma_i$ for the single material problem. In Fig. 12, the single material result considering material 1 is shown and the volume fraction and compliance are reported. In Fig. 13, the single material results considering materials 2a, 2b, 2c, and 2d are shown and the associated volume fractions and compliance values are reported. Note that the volume fractions are consistent with those required by the mass constraint, i.e., the volume fraction of material 1 is $0.35/\gamma_1 = 0.35$ and the volume fractions of material 2 are $0.35/\gamma_2 = 0.700, 0.714, 0.729, 0.745$ for cases a, b, c, and d, respectively. In all cases, the volume of material 2 is greater than that of material 1 since material 2 has a lower mass density in all cases. Although material 1 is stiffer than material 2, the compliance of the structure composed of only material 2 becomes more efficient (lower objective) once the mass density of material 2 becomes large and there is enough allowable volume to make up for the reduced stiffness.

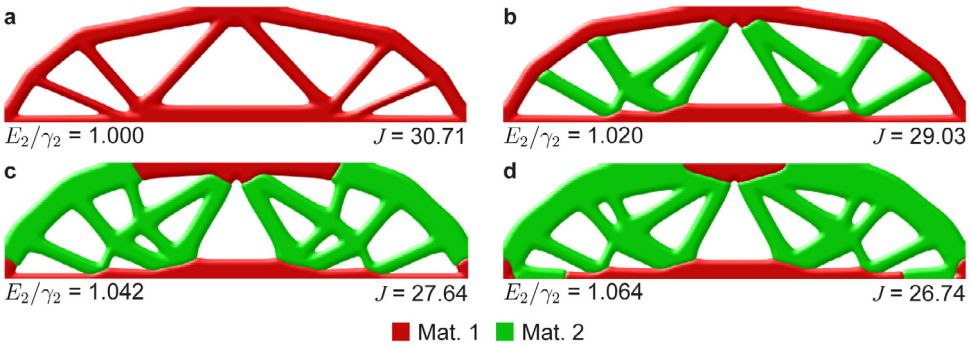

Fig. 14. 2-material MBB beam design with $E_1/\gamma_1 = 1$ and varying stiffness-to-mass ratio for material 2: (a) $E_2/\gamma_2 = 1.000$; (b) $E_2/\gamma_2 = 1.020$; (c) $E_2/\gamma_2 = 1.042$; (d) $E_2/\gamma_2 = 1.064$. Plotted material distributions are based on the converged results (i.e., before post-processing) (color online).

Table 10
Volume fractions, constraint, g, and compliance, J, for each of the composite MBB beam designs considering candidate materials 1 and 2 and a single global mass constraint ($M^{max}/V^{total} = 0.35$) with $E_1/\gamma_1 = 1$ ($E_1 = 1$, $\gamma_1 = 1$) and varying stiffness to mass-ratio for material 2. All numerical results are based on the converged results (i.e., before post-processing).

Fig.						Volume fraction			g_1	J
	E_1	γ_1	E_2	γ_2	E_2/γ_2	Mat. 1	Mat. 2	Total		
14(a)	1.000	1.000	0.500	0.500	1.000	0.350	0.000	0.350	0.000	30.71
14(b)	1.000	1.000	0.500	0.490	1.020	0.250	0.205	0.455	0.000	29.03
14(c)	1.000	1.000	0.500	0.480	1.042	0.153	0.411	0.564	0.000	27.64
14(d)	1.000	1.000	0.500	0.470	1.064	0.119	0.493	0.611	0.000	26.74

Next, the 2-material problems described in Table 9 are considered to determine whether multi-material designs will perform better than the single material designs in Figs. 12 and 13. The resulting designs are plotted in Fig. 14 and the corresponding volume fractions, constraint values, and compliance values are provided in Table 10. When the stiffness-to-mass ratios of materials 1 and 2 are equal (Fig. 14(a)), the stiffer material is selected, as expected. As the stiffness-to-mass ratio of material 2 becomes larger (Fig. 14(b), (c), (d)), an increasing volume of the material 2 arises. Note that in all cases, the compliance is less than or equal to that of the single material designs in Figs. 12 and 13.[2] *Thus, for the considered mass constrained problem, a multi-material design tends to be more efficient when the stiffness-to-mass ratio of the less stiff material becomes large enough that the increased allowable volume makes up for its reduced stiffness.*

6.3. Controlling the void distribution with multiple local volume constraints

In this section, a domain of width 90 and height 240 is designed considering a single material ($E_1 = 1$, $\nu_1 = 0.3$) and local volume constraints are defined to control sub-regions of the domain, i.e., the constraints are local. Five cases are considered: one, six, twelve, twenty-four, and ninety-six sub-regions (see Fig. 15), each with a volume constraint limiting the material from occupying more than 50% of the sub-region volume. In each case, the boundary conditions of Fig. 15(a) are applied: fixed support at the base and eleven equal point loads of magnitude 0.1 applied along the height of the domain on both sides. The same finite element discretization is used in all cases: 90×240, four-node quadrilateral finite elements.

The resulting designs are provided in Fig. 16, where it is shown that for a single sub-region (Fig. 16(a)) the material tends to concentrate in the bottom half of the structure and as the number of specified sub-regions increases, the material becomes more uniformly distributed throughout the domain. Designs of this nature, with many intricate

[2] The difference in compliance, J, between the designs in Figs. 12 and 14(a) is a numerical artifact resulting from the fact that one is a single material optimization problem and the other is a multi-material optimization problem, i.e., the two problems have different numbers of design variables and different initial guesses.

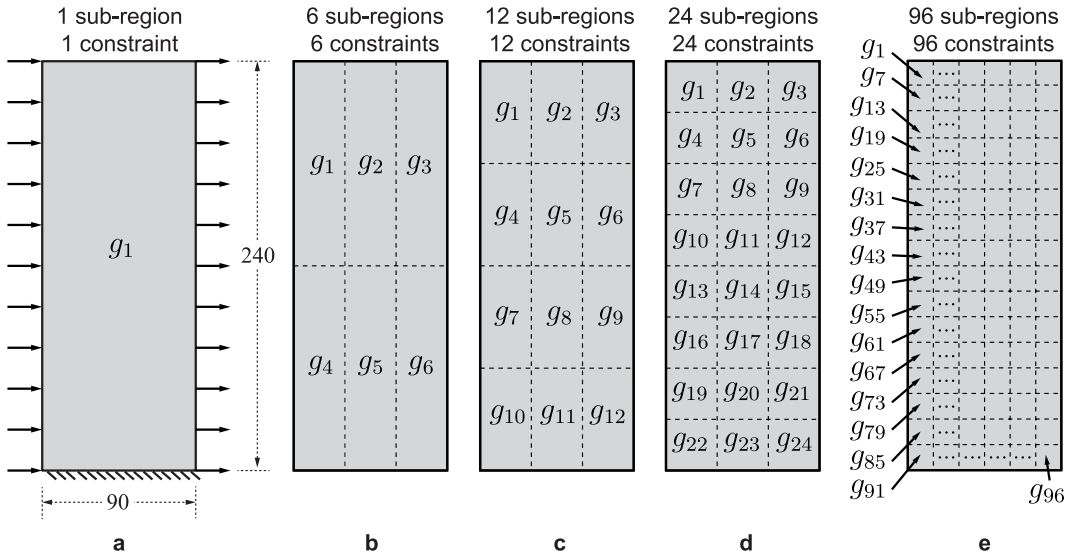

Fig. 15. Exploring local volume constraints: (a) domain and boundary conditions with one sub-region; (b) six sub-regions; (c) twelve sub-regions; (d) twenty-four sub-regions; and (e) ninety-six sub-regions, each controlled by a single volume constraint with one candidate material.

details and redundancies, may be desirable in a number of applications.[3] Note that the volume fraction of material (of the entire domain) is equal to 0.5 in each of the final designs in Fig. 16, but the compliance increases as the number of sub-regions increases and the problem becomes highly constrained (see the convergence plots in Fig. 17).

6.4. 3D cantilever beam

The presented formulation is also implemented in a modified version of the 3D MATLAB code provided by Liu and Tovar [53]. Here, a 3D cantilever beam with a vertical point load at the tip is designed considering two volume constraints, each controlling a single material in the entire domain. The domain and boundary conditions are provided in Fig. 18, where the length parameter L is taken to be 64 and P is a unit load. The $192 \times 64 \times 64$ domain is discretized into 786,432 eight-node hexahedral elements with unit edge length. Material properties for the two candidate materials are provided in Table 11 along with the volume limits for the two constraints. Optimization parameters specified for the 3D cantilever are provided in Table 2. Continuation on the SIMP penalty parameter, p, is often considered in 2-phase topology optimization to bias the solution toward that of the convex problem ($p = 1$) in the first few iterations. Although the material interpolation used here does not guarantee a convex problem for $p = 1$, continuation is effective in achieving desirable designs, perhaps due to the fact that the material interpolation is similar to the standard 2-phase SIMP interpolation when no mixing exists in the design. As such, $p = 1$ is used at the start of the algorithm and is incremented by 0.5 every ten iterations until $p = 3$, at which point p remains constant until convergence.

The final design after post-processing (technique #1, i.e., all mixing eliminated) as well as a 3D-printed version of the design are provided in Fig. 19. The 3D-print was manufactured using an ink-jet technology to bond layers of plaster-like powder together (zp®151 Powder) with a colored bonding agent (ColorBond zbond®90).[4,5] The post-processed design was prepared for 3D printing using TOPslicer [7] (modified to accommodate multiple materials) to generate an X3D file containing both volume and color data, where the different colors represent the different materials.

[3] In the case of building bracing design, specifying local volume constraints may enable the designer to achieve designs in which more uniform lighting is emitted into the interior space. Local volume constraints may also be useful for design of biological structures, which often have complex microstructures [52].

[4] The model was printed using an online 3D-printing service from Sculpteo.

[5] Printer: Z Corporation ZPrinter 650.

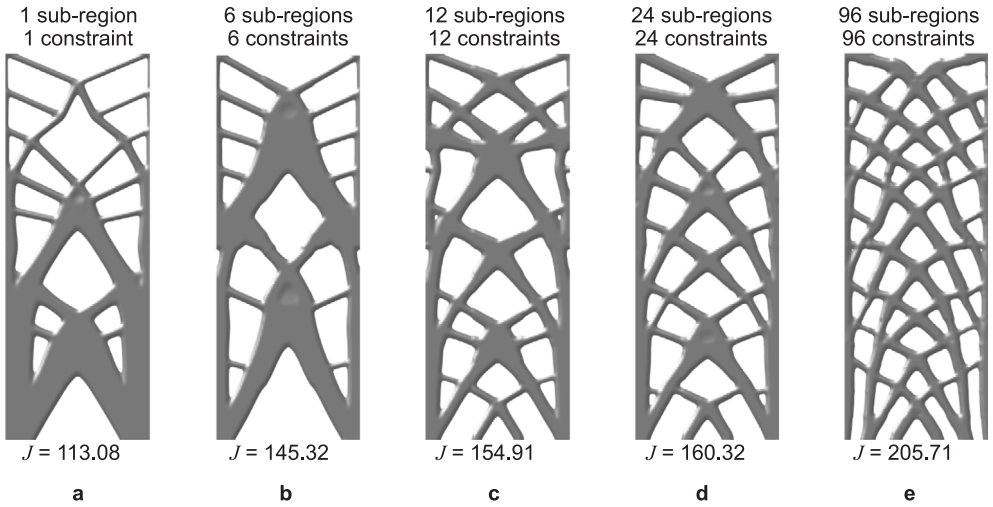

Fig. 16. Designs considering local volume constraints: (a) one sub-region; (b) six sub-regions; (c) twelve sub-regions; (d) twenty-four sub-regions; and (e) ninety-six sub-regions, each controlled by a single volume constraint with one candidate material.

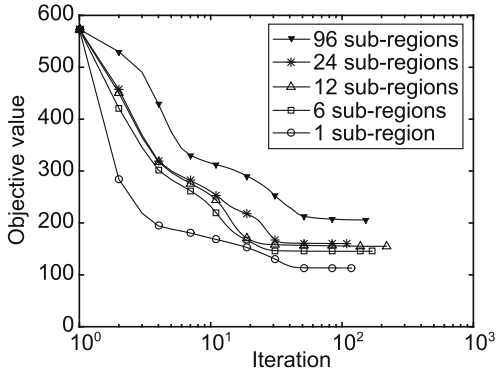

Fig. 17. Objective value vs. iteration for single-material designs with many local volume constraints.

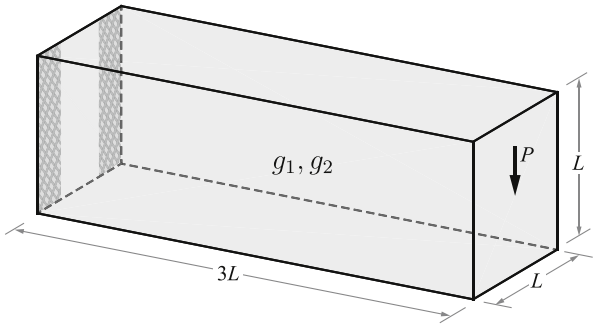

Fig. 18. Cantilever domain and boundary conditions.

7. Conclusions

A simple and robust formulation for multi-material topology optimization in the continuum setting is presented that can accommodate an arbitrary number of candidate materials and arbitrarily specified volume/mass constraints

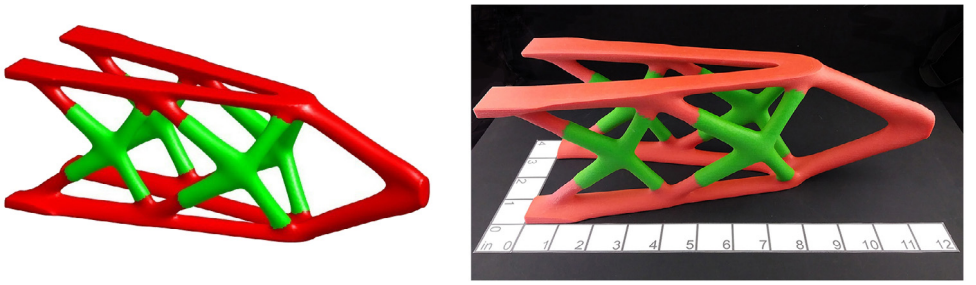

Fig. 19. 3D cantilever design based on two volume constraints, each controlling a single candidate material in the entire domain: (a) numerical result after post-processing (technique #1); (b) 3D printed model that visualizes the material distribution using color (color online).

Table 11
Candidate materials associated with each of the two volume constraints for the problem depicted in Fig. 18 considering Poisson's ratio $\nu_i = 0.3$ (constant), $i = 1, \ldots, 10$.

Mat.	E_i	Constraints	
		g_1	g_2
1	1	✓	–
2	0.5	–	✓
Volume fraction:		0.07	0.03

(global and/or local constraints). Specifically, by taking advantage of the separable dual objective in the linearized subproblems, the ZPR scheme updates for each volume/mass constraint independently. As such, the formulation is effective for multiple volume/mass constraints that can control all or a subset of the candidate materials in the entire domain or a subset of the domain. Although the selected DMO material interpolation causes the number of design variables to increase linearly with the number of candidate materials, the variable separability of constraints defined in accordance with the DMO material interpolation lends them to being coupled with the efficient ZPR update scheme. Although additional constraints to ensure that pointwise densities do not exceed one are not considered, it is shown that a simple post-processing step is sufficient to achieve physical designs that have similar behavior as the converged designs.

The formulation itself places no limits on the number of candidate materials. Results with up to ten solid material phases are presented and the formulation is shown to achieve designs (local minima) in agreement with human intuition from the perspective of mechanics. It is also shown that by specifying volume constraints on sub-regions of the domain (local constraints), a designer can obtain increased control over the material distribution, at the expense of increased compliance for a more highly constrained problem.

Lastly, the formulation is demonstrated in 3D and the result is 3D-printed using multiple colors to visually represent the various materials. Although the 3D-printed model provided here is not functional, it demonstrates that technologies for realizing designs with varying elastic properties may be achieved using similar ideas as the multicolor print.[6] Perhaps more nearsighted future work would be to consider cellular and/or anisotropic candidate materials and obtain designs with varying material properties from a single bulk material [11,55,57]. In fact, the multi-material formulation presented here is available as part of Sandia National Laboratories' PLATO code, an object-oriented, massively parallel framework for optimization-based design, which can accommodate anisotropic and cellular materials [8,56]. Thus, the PLATO implementation can be seen as an avenue toward designing structures with varying material properties that are practical to manufacture.

[6] This possibility can be explored as the appropriate technologies, e.g., PolyJet [10] or others [54], improve and new technologies become available.

Acknowledgments

The authors acknowledge the financial support from the US National Science Foundation (NSF) under projects #1559594 and #1663244. We are also grateful for the endowment provided by the Raymond Allen Jones Chair at the Georgia Institute of Technology. In addition, Sandia National Laboratories is a multimission laboratory managed and operated by National Technology and Engineering Solutions of Sandia, LLC, a wholly owned subsidiary of Honeywell International, Inc., for the U.S. Department of Energy's National Nuclear Security Administration under contract DE-NA0003525. Lastly, we thank Anderson Pereira for providing insightful feedback that greatly improved the manuscript. The information provided in this paper is the sole opinion of the authors and does not necessarily reflect the views of the sponsoring agencies.

Appendix. Nomenclature

Γ_D	Partition of $\partial\Omega$ where displacements are prescribed
Γ_N	Partition of $\partial\Omega$ where tractions are applied
$\tilde{\Gamma}_N$	Partition of Γ_N where non-zero tractions are applied
$\mathbf{H}$	Matrix of linear density filter weights
Ω	Set of material points in design domain
α	Linearization exponent
χ	Indicator function
δ	ZPR move limit
$\partial\Omega$	Boundary of Ω
$\delta\mathbf{u}$	Test functions
η	Material interpolation function
γ_i	Scale factor representing mass density of material i
λ_j	Lagrange multiplier of constraint j
ν_i	Poisson's ratio of material i
ω	Set of material points defining optimal shape
$\rho_T(\mathbf{X})$	Total density of material at material point $\mathbf{X}$
ρ_T^e	Total density of material in element e
$\hat{\rho}_i$	Filtered density field of material i
$\rho_i(\mathbf{X})$	Continuous density field for material i
E_i	Modulus of elasticity associated with material i
E_{min}	Ersatz stiffness
F	Filter
J	Objective function (structural compliance)
N	Number of elements in design domain
M_j^{max}	Mass limit associated with constraint j
N_c	Number of volume/mass constraints
N_i	Shape function for degree of freedom i
R	Filter radius
S	Set of material tensors
U	Set of kinematically admissible displacement fields
U_o	Set of test functions
V^e	Volume of element e
V_T^e	Total volume of material in element e
V_j^{max}	Volume limit associated with constraint j
V^{total}	Total domain volume
$\mathbf{C}(\mathbf{X})$	Spatially varying material tensor
$\mathbf{K}$	Stiffness matrix
$\mathbf{X} \in \mathbb{R}^{n_{sd}}$	Material point
$\mathbf{f}$	Vector of applied nodal forces
$\mathbf{k}^e$	Element stiffness matrix

$\mathbf{k}_o^e$ Constant portion of element stiffness matrix
$\mathbf{u}$ Displacement field (trial functions)
$\mathbf{y}_i$ Intervening variable
$d\,(j, e)$ Distance between design variables z_i^j and z_i^e
g_j jth volume/mass constraint
m Number of candidate materials available in the domain
n_d Spatial dimension
n_n Number of nodes per element
p Penalty parameter for SIMP
q Penalty parameter for RAMP
$\mathbf{t}$ Traction
w_i^e Weight of material i in element e
z_i^e Design variable associated with material i in element e
$\hat{z}_i^e$ Filtered density of material i in element e
ZPR Zhang–Paulino–Ramos Jr. design variable update scheme, pronounced "zipper"
$\bar{\mathbf{t}}$ Prescribed traction
$\bar{\mathbf{u}}$ Prescribed displacement
$\underline{z}_i^e, \overline{z}_i^e$ Lower and upper bounds on z_i^e during the design variable update
$\tilde{z}_i^e$ Filtered and penalized density of material i in element e
$\mathcal{A}$ Choice function
$\mathcal{D}_j$ Set of design variables associated with constraint j
$\mathcal{E}_j$ Set of element indices associated with constraint j
$\mathcal{G}_j$ Set of material indices associated with constraint j
$\mathcal{N}_e$ Neighborhood of element e

References

[1] X.S. Zhang, G.H. Paulino, A.S. Ramos Jr., Multi-material topology optimization with multiple volume constraints: A general approach applied to ground structures with material nonlinearity, Struct. Multidiscip. Optim. 57 (2018) 161–182.
[2] T. Gao, W. Zhang, A mass constraint formulation for structural topology optimization with multiphase materials, Internat. J. Numer. Methods Engrg. 88 (8) (2011) 774–796.
[3] Y. Wang, Z. Luo, Z. Kang, N. Zhang, A multi-material level set-based topology and shape optimization method, Comput. Methods Appl. Mech. Engrg. 283 (2015) 1570–1586.
[4] A.M. Mirzendehdel, K. Suresh, A Pareto-optimal approach to multimaterial topology optimization, J. Mech. Des. 137 (10) (2015) 101701.
[5] A.H. Taheri, K. Suresh, An isogeometric approach to topology optimization of multi-material and functionally graded structures, Internat. J. Numer. Methods Engrg. 109 (5) (2017) 668–696.
[6] W. Zuo, K. Saitou, Multi-material topology optimization using ordered SIMP interpolation, Struct. Multidiscip. Optim. 55 (2017) 477–491.
[7] T. Zegard, G.H. Paulino, Bridging topology optimization and additive manufacturing, Struct. Multidiscip. Optim. 53 (1) (2016) 175–192.
[8] J. Robbins, S.J. Owen, B.W. Clark, T.E. Voth, An efficient and scalable approach for generating topologically optimized cellular structures for additive manufacturing, Addit. Manuf. 12 (2016) 296–304.
[9] A.T. Gaynor, N.A. Meisel, C.B. Williams, J.K. Guest, Multiple-material topology optimization of compliant mechanisms created via polyjet three-dimensional printing, J. Manuf. Sci. Eng. 136 (6) (2014) 061015.
[10] Stratasys. PolyJet Materials: A rangle of possibilities. Technical report, 2016.
[11] C. Schumacher, B. Bickel, J. Rys, S. Marschner, C. Daraio, M. Gross, Microstructures to control elasticity in 3D printing, ACM Trans. Graph. 34 (4) (2015) 136:1–136:13.
[12] M.P. Bendsøe, Optimal shape design as a material distribution problem, Struct. Optim. 1 (4) (1989) 193–202.
[13] M. Zhou, G.I.N. Rozvany, The COC algorithm, Part II: topological, geometrical and generalized shape optimization, Comput. Methods Appl. Mech. Engrg. 89 (1–3) (1991) 309–336.
[14] O. Sigmund, S. Torquato, Design of materials with extreme thermal expansion using a three-phase topology optimization method, J. Mech. Phys. Solids 45 (6) (1997) 1037–1067.
[15] O. Sigmund, Design of multiphysics actuators using topology optimization–Part II: Two-material structures, Comput. Methods Appl. Mech. Engrg. 190 (49) (2001) 6605–6627.
[16] S.L. Vatanabe, G.H. Paulino, E.C.N. Silva, Influence of pattern gradation on the design of piezocomposite energy harvesting devices using topology optimization, Composites B 43 (6) (2012) 2646–2654.

[17] S.L. Vatanabe, G.H. Paulino, E.C.N. Silva, Design of functionally graded piezocomposites using topology optimization and homogenization–Toward effective energy harvesting materials, Comput. Methods Appl. Mech. Engrg. 266 (2013) 205–218.
[18] S.L. Vatanabe, G.H. Paulino, E.C.N. Silva, Maximizing phononic band gaps in piezocomposite materials by means of topology optimization, J. Acoust. Soc. Am. 136 (2) (2014) 494–501.
[19] A.H. Taheri, B. Hassani, Simultaneous isogeometrical shape and material design of functionally graded structures for optimal eigenfrequencies, Comput. Methods Appl. Mech. Engrg. 277 (2014) 46–80.
[20] J. Stegmann, E. Lund, Discrete material optimization of general composite shell structures, Internat. J. Numer. Methods Engrg. 62 (14) (2005) 2009–2027.
[21] L.V. Gibiansky, O. Sigmund, Multiphase composites with extremal bulk modulus, J. Mech. Phys. Solids 48 (3) (2000) 461–498.
[22] E. Lund, J. Stegmann, On structural optimization of composite shell structures using a discrete constitutive parametrization, Wind Energy 8 (1) (2005) 109–124.
[23] C.F. Hvejsel, E. Lund, Material interpolation schemes for unified topology and multi-material optimization, Struct. Multidiscip. Optim. 43 (6) (2011) 811–825.
[24] C.F. Hvejsel, E. Lund, M. Stolpe, Optimization strategies for discrete multi-material stiffness optimization, Struct. Multidiscip. Optim. 44 (2) (2011) 149–163.
[25] R. Tavakoli, S.M. Mohseni, Alternating active-phase algorithm for multimaterial topology optimization problems: a 115-line matlab implementation, Struct. Multidiscip. Optim. 49 (4) (2014) 621–642.
[26] J. Park, A. Sutradhar, A multi-resolution method for 3D multi-material topology optimization, Comput. Methods Appl. Mech. Engrg. 285 (2015) 571–586.
[27] E.T. Filipov, J. Chun, G.H. Paulino, J. Song, Polygonal multiresolution topology optimization (PolyMTOP) for structural dynamics, Struct. Multidiscip. Optim. 53 (4) (2016) 673–694.
[28] T.H. Nguyen, G.H. Paulino, J. Song, C.H. Le, A computational paradigm for multiresolution topology optimization (MTOP), Struct. Multidiscip. Optim. 41 (4) (2010) 525–539.
[29] T.H. Nguyen, G.H. Paulino, J. Song, C.H. Le, Improving multiresolution topology optimization via multiple discretizations, Internat. J. Numer. Methods Engrg. 92 (6) (2012) 507–530.
[30] Q.X. Lieu, J. Lee, A multi-resolution approach for multi-material topology optimization based on isogeometric analysis, Comput. Methods Appl. Mech. Engrg. 323 (2017) 272–302.
[31] Thomas J.R. Hughes, John A. Cottrell, Yuri Bazilevs, Isogeometric analysis: CAD, finite elements, NURBS, exact geometry and mesh refinement, Comput. Methods Appl. Mech. Engrg. 194 (39) (2005) 4135–4195.
[32] Q.H. Doan, D. Lee, Optimum topology design of multi-material structures with non-spurious buckling constraints, Adv. Eng. Softw. 114 (2017) 110–120.
[33] K.N. Chau, K.N. Chau, T. Ngo, K. Hackl, H. Nguyen-Xuan, A polytree-based adaptive polygonal finite element method for multi-material topology optimization, Comput. Methods Appl. Mech. Engrg. 332 (2018) 712–739.
[34] L. Yin, G.K. Ananthasuresh, Topology optimization of compliant mechanisms with multiple materials using a peak function material interpolation scheme, Struct. Multidiscip. Optim. 23 (1) (2001) 49–62.
[35] M.Y. Wang, X. Wang, Color level sets: a multi-phase method for structural topology optimization with multiple materials, Comput. Methods Appl. Mech. Engrg. 193 (6) (2004) 469–496.
[36] M.Y. Wang, S. Chen, X. Wang, Y. Mei, Design of multimaterial compliant mechanisms using level-set methods, J. Mech. Des. 127 (5) (2005) 941–956.
[37] X. Guo, W. Zhang, W. Zhong, Stress-related topology optimization of continuum structures involving multi-phase materials, Comput. Methods Appl. Mech. Engrg. 268 (2014) 632–655.
[38] M.Y. Wang, S. Zhou, Synthesis of shape and topology of multi-material structures with a phase-field method, J. Comput.-Aided Mater. Des. 11 (2–3) (2004) 117–138.
[39] S. Zhou, M.Y. Wang, Multimaterial structural topology optimization with a generalized Cahn–Hilliard model of multiphase transition, Struct. Multidiscip. Optim. 33 (2) (2007) 89–111.
[40] R. Tavakoli, Multimaterial topology optimization by volume constrained Allen–Cahn system and regularized projected steepest descent method, Comput. Methods Appl. Mech. Engrg. 276 (2014) 534–565.
[41] M. Wallin, N. Ivarsson, M. Ristinmaa, Large strain phase-field-based multi-material topology optimization, Internat. J. Numer. Methods Engrg. 104 (9) (2015) 887–904.
[42] X. Huang, Y.M. Xie, Bi-directional evolutionary topology optimization of continuum structures with one or multiple materials, Comput. Mech. 43 (3) (2009) 393–401.
[43] C. Talischi, G.H. Paulino, A. Pereira, I.F.M. Menezes, PolyTop: a Matlab implementation of a general topology optimization framework using unstructured polygonal finite element meshes, Struct. Multidiscip. Optim. 45 (3) (2012) 329–357.
[44] M. Stolpe, K. Svanberg, An alternative interpolation scheme for minimum compliance optimization, Struct. Multidiscip. Optim. 22 (2) (2001) 116–124.
[45] B. Bourdin, Filters in topology optimization, Internat. J. Numer. Methods Engrg. 50 (9) (2001) 2143–2158.
[46] O. Sigmund, A 99 line topology optimization code written in matlab, Struct. Multidiscip. Optim. 21 (2) (2001) 120–127.
[47] M. Bruyneel, SFP —a new parameterization based on shape functions for optimal material selection: application to conventional composite plies, Struct. Multidiscip. Optim. 43 (1) (2011) 17–27.
[48] P.W. Christensen, A. Klarbring, An Introduction to Structural Optimization, Springer, Linköping, 2009.
[49] M.P. Bendsøe, O. Sigmund, Topology Optimization: Theory, Methods, and Applications, Springer, 2003.

[50] K. Svanberg, The method of moving asymptotes-A new method for structural optimization, Internat. J. Numer. Methods Engrg. 24 (1987) 359–373.
[51] A.A. Groenwold, L.F.P. Etman, On the equivalence of optimality criterion and sequential approximate optimization methods in the classical topology layout problem, Internat. J. Numer. Methods Engrg. 73 (3) (2008) 297–316.
[52] U.G.K. Wegst, H. Bai, E. Saiz, A.P. Tomsia, R.O. Ritchie, Bioinspired structural materials, Nature Mater. 14 (1) (2015) 23–36.
[53] K. Liu, A. Tovar, An efficient 3D topology optimization code written in Matlab, Struct. Multidiscip. Optim. 50 (6) (2014) 1175–1196.
[54] D.L. Bourell, Perspectives on additive manufacturing, Annu. Rev. Mater. Res. 46 (2016) 1–18.
[55] T.A. Schaedler, W.B. Carter, Architected cellular materials, Annu. Rev. Mater. Res. 46 (2016) 187–210.
[56] Sandia National Laboratories. Plato. 2017. http://www.sandia.gov/plato3d/index.html (Accessed: 06.12.16).
[57] F. Regazzoni, N. Parolini, M. Verani, Topology optimization of multiple anisotropic materials, with application to self-assembing diblock copolymers, 2017. arXiv preprint arXiv:1711.10784.